



The Ionized Warped Disk and Disk Wind of the Massive Protostar Monoceros R2-IRS2 Seen with ALMA

Izaskun Jiménez-Serra¹ , Alejandro Báez-Rubio¹, Jesús Martín-Pintado¹, Qizhou Zhang² , and Víctor M. Rivilla³

¹ Centro de Astrobiología (CSIC-INTA), Ctra. de Torrejón a Ajalvir km 4, E-28850, Torrejón de Ardoz, Spain; ijimenez@cab.inta-csic.es

² Center for Astrophysics, Harvard & Smithsonian, 60 Garden St., Cambridge, MA 02138, USA

³ INAF-Osservatorio Astrofisico di Arcetri, Largo E. Fermi 5, I-50125 Firenze, Italy

Received 2020 May 27; revised 2020 June 25; accepted 2020 June 26; published 2020 July 13

Abstract

Theories of massive star formation predict that massive protostars accrete gas through circumstellar disks. Although several cases have been found already thanks to high angular-resolution interferometry, the internal physical structure of these disks remains unknown, in particular whether they present warps or internal holes, as observed in low-mass protoplanetary disks. Here, we report very high angular-resolution observations of the H21 α radio recombination line carried out in Band 9 with the Atacama Large Millimeter/submillimeter Array (beam of 80 mas \times 60 mas, or 70 au \times 50 au) toward the IRS2 massive young stellar object in the Monoceros R2 star-forming cluster. The H21 α line shows maser amplification, which allows us to study the kinematics and physical structure of the ionized gas around the massive protostar down to spatial scales of ~ 1 –2 au. Our ALMA images and 3D radiative transfer modeling reveal that the ionized gas around IRS2 is distributed in a Keplerian circumstellar disk and an expanding wind. The H21 α emission centroids at velocities between -10 and 20 km s $^{-1}$ deviate from the disk plane, suggesting a warping for the disk. This could be explained by the presence of a secondary object (a stellar companion or a massive planet) within the system. The ionized wind seems to be launched from the disk surface at distances ~ 11 au from the central star, consistent with magnetically-regulated disk wind models. This suggests a similar wind-launching mechanism to that recently found for evolved massive stars such as MWC349A and MWC922.

Unified Astronomy Thesaurus concepts: [Star formation \(1569\)](#)

1. Introduction

The formation processes of massive stars (with masses $\geq 8 M_{\odot}$) are under debate. Massive stars could form either by the monolithic collapse of a turbulent molecular core (McKee & Tan 2002), by the competitive accretion of core materials (Bonnell & Bate 2006), or by Bondi–Hoyle accretion onto the central star (Keto 2007). In all these theories, gas accretion occurs through a circumstellar disk coupled with an expanding wind/outflow (which removes angular momentum), in a scaled-up version of low-mass star formation. High angular-resolution interferometry has unveiled several cases of circumstellar disks around massive protostars such as Cepheus A HW2 (Patel et al. 2005; Jiménez-Serra et al. 2007, 2009), IRAS 20126+4104 (Cesaroni et al. 2014; Chen et al. 2016), G17.64+0.16 (Maud et al. 2019), or GGD 27-MM1 (Añez-López et al. 2020). However, the level of detail in these observations only goes down to 40 au (Maud et al. 2019; Añez-López et al. 2020), insufficient to probe the innermost structure of these disks. Hints of holes have recently been reported (Maud et al. 2019), but it remains unknown whether warps exist within these disks as found for their low-mass counterparts (Sakai et al. 2019; Kraus et al. 2020; Sai et al. 2020). The launching process of winds/outflows has not been witnessed either during the protostellar phase of massive stars.⁴

Hydrogen radio recombination lines (RRLs) probe the kinematics of the ionized gas in ultracompact (UC) H II regions during the process of massive star formation

(Churchwell 2002). About 30% of these regions show broad RRLs with line widths ≥ 60 –80 km s $^{-1}$, which exceed those produced by just thermal broadening (FWHM ~ 30 km s $^{-1}$; Churchwell 2002). These regions show elongated morphologies and thus broad RRL emission likely arises from ionized winds (Jaffe & Martín-Pintado 1999).

Non-LTE effects such as maser amplification are expected in RRLs. These effects are pronounced in transitions at submillimeter wavelengths when electron densities reach values $n_e \sim 10^6$ – 10^8 cm $^{-3}$ (Figure 5 in Streltnitski et al. 1996). However, RRL masers are rare. Only a few objects have been detected so far, such as MWC349A (Martín-Pintado et al. 1989a; Báez-Rubio et al. 2013), η Carinae (Cox et al. 1995), or the evolved B[e]-type massive star MWC922 (Sánchez Contreras et al. 2019). Thanks to their brightness, the kinematics of the innermost ionized regions toward these evolved objects can be measured with accuracies down to a few astronomical units (Weintraub et al. 2008; Martín-Pintado et al. 2011; Báez-Rubio et al. 2013; Zhang et al. 2017). This has revealed that they not only present circumstellar disks rotating following a Keplerian law, but also that ionized winds are launched from their disks at radii $\lesssim 25$ –30 au (Martín-Pintado et al. 2011; Sánchez Contreras et al. 2019). Unfortunately, similar studies do not exist for massive protostellar objects.

Monoceros R2 (hereafter MonR2) is a massive star-forming cluster located at a distance of 893 pc (Dzib et al. 2016). It hosts a blister-type H II region and a cluster of IR sources (Massi et al. 1985; Wood & Churchwell 1989; Carpenter et al. 1997; Treviño-Morales et al. 2019). Among them, IRS2 is a compact and massive young stellar object with a luminosity ~ 0.5 – $1 \times 10^4 L_{\odot}$ (Howard et al. 1994; Álvarez et al. 2004). High angular-resolution observations carried out with the

⁴ The protostellar nature of the emission line star MWC349A is highly debated (Hartmann et al. 1980; Gvaramadze & Menten 2012; Streltnitski et al. 2013; Zhang et al. 2017). The latest results suggest that this object is an evolved B[e] supergiant (Kraus et al. 2020).

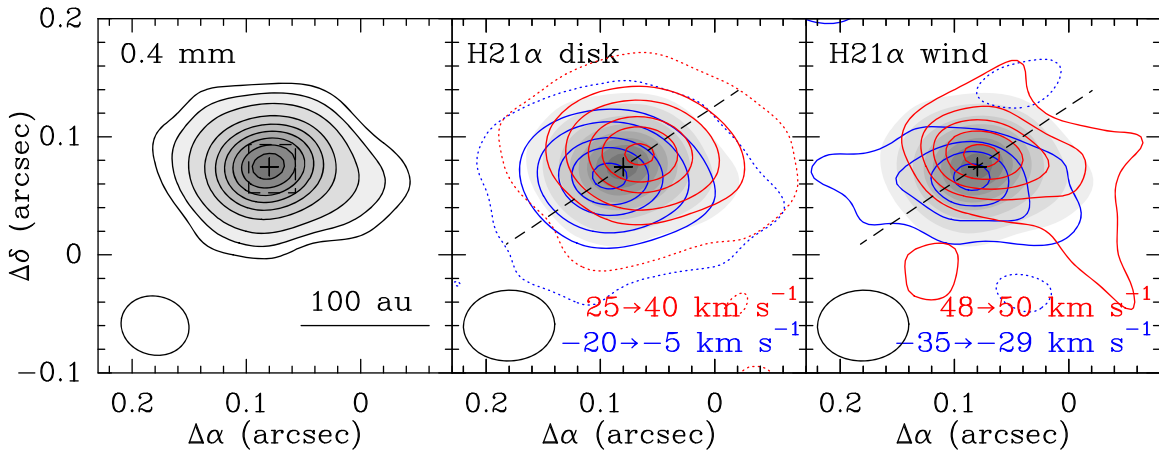


Figure 1. Left panel: 0.4 mm continuum map measured toward MonR2-IRS2 with ALMA. Contours correspond to 3σ , 6σ , 12σ , 24σ , 36σ , 48σ , 60σ , 72σ , and 84σ , with $1\sigma = 1.9 \text{ mJy beam}^{-1}$. The cross indicates the continuum peak. The dashed box shows the region of the H21 α centroid map of Figure 3. Middle panel: H21 α integrated intensity maps obtained for the ionized disk between 25 and 40 km s^{-1} (red) and -20 and -5 km s^{-1} (blue). Contours correspond to the 3σ (dotted lines), 20σ , 40σ , 80σ , 110σ , and 150σ levels, with $1\sigma = 160 \text{ mJy beam}^{-1} \text{ km s}^{-1}$, for both the redshifted and blueshifted parts of the disk. The grayscale image shows the continuum emission. The dashed line indicates the disk plane. Right panel: H21 α maps of the high-velocity gas obtained between 48 and 50 km s^{-1} (contours at 2σ , 5σ , 7.5σ , and 10σ , and 12.5σ , with $1\sigma = 42 \text{ mJy beam}^{-1} \text{ km s}^{-1}$). The grayscale and dashed line are the same as those in the middle panel. ALMA beams are shown in the lower left corner of each panel.

Submillimeter Array (SMA) revealed that MonR2-IRS2 is a UC H II region with its RRLs at $\lambda \leq 0.85 \text{ mm}$ experiencing maser amplification. However, these observations were unable to resolve the internal structure of the source (Jiménez-Serra et al. 2013).

We present high angular-resolution observations ($80 \text{ mas} \times 60 \text{ mas}$, $70 \text{ au} \times 50 \text{ au}$) of the H21 α RRL carried out with the Atacama Large Millimeter/submillimeter Array (ALMA) toward the MonR2-IRS2 UC H II region. Our H21 α images show that the ionized gas in MonR2-IRS2 is distributed in a warped Keplerian disk and an ionized wind that is launched at radii $\sim 11 \text{ au}$.

2. Observations

The H21 α RRL at 662.40416 GHz was observed on 2015 September 25 with ALMA in Band 9 (project 2012.1.00522.S) using the 12 m array (baselines from 43 m to 2.27 km). Observations were performed in dual polarization mode using a spectral bandwidth of 1.875 GHz and a spectral resolution of 976 kHz (0.44 km s^{-1}). As calibrators, J0522–3627 was used for bandpass calibration, J0423–013 for flux calibration, and J0607–0834 for phase and amplitude calibration.

The calibrated data set was obtained by running the original pipeline reduction scripts, and the data were additionally self-calibrated using the CASA (the Common Astronomy Software Applications) package version 5.0.0. The MonR2-IRS2 spectra are clean from molecular emission, thus the 0.4 mm continuum map was generated using the CASA task *uvcontsub* across 5.61 GHz of line-free bandwidth. The angular resolution of the 0.4 mm continuum image was $60 \text{ mas} \times 50 \text{ mas}$, P.A. = 78° and the rms noise level was $1.9 \text{ mJy beam}^{-1}$. The H21 α image was obtained from the continuum-subtracted data cube after smoothing the velocity resolution to 1 km s^{-1} . The beam and rms noise level of the H21 α image were $80 \text{ mas} \times 60 \text{ mas}$, P.A. = -88° , and 30 mJy beam^{-1} in 1 km s^{-1} -channels, respectively.

3. Results

3.1. 0.4 mm Continuum Emission

Figure 1 (left panel) reports the 0.4 mm continuum map obtained toward MonR2-IRS2 (black contours and grayscale). The source is barely resolved at the resolution of ALMA (deconvolved size $62 \text{ mas} \times 43 \text{ mas}$, or $55 \text{ au} \times 38 \text{ au}$). Its morphology clearly deviates from Gaussianity at the low-emission level ($\leq 12\sigma$, with $1\sigma = 1.9 \text{ mJy beam}^{-1}$), likely due to the presence of a wind (Section 4). By fitting a 2D Gaussian to the continuum emission, the peak coordinates of MonR2-IRS2 are $\alpha(\text{J2000}) = 06^{\text{h}}07^{\text{m}}45^{\text{s}}.8034 (\pm 0^{\text{s}}.0008)$, $\delta(\text{J2000}) = -06^{\circ}22'53''.5155 (\pm 0''.0005)$, which are consistent with the previously measured values (Jiménez-Serra et al. 2013).

The integrated continuum flux at 0.4 mm is $(345 \pm 10) \text{ mJy}$. This value is larger than that expected from the spectral index of $\alpha = -0.16 \pm 0.2$ measured by the SMA (with $S \propto \nu^\alpha$; Jiménez-Serra et al. 2013).⁵ The free-free contribution is $130 \pm 30 \text{ mJy}$; thus while the continuum emission at $\lambda \geq 0.85 \text{ mm}$ is entirely due to ionized gas, the $\lambda = 0.4 \text{ mm}$ continuum flux is dominated by dust. The mass for the neutral disk can then be estimated using a dust flux of $215 \pm 32 \text{ mJy}$ and by assuming dust temperatures $T_{\text{dust}} = 500\text{--}1200 \text{ K}$ (Howard et al. 1994), a gas-to-dust mass ratio $R = 100$, and a dust opacity $\kappa_{\text{dust}} = 25.8 \text{ cm}^2 \text{ g}^{-1}$ (consistent with H_2 gas densities of 10^8 cm^{-3} and no ices; Ossenkopf & Henning 1994). The neutral disk mass is $\sim 2\text{--}4 \times 10^{-4} M_\odot$, with a 15% uncertainty.

3.2. H21 α Maser Emission

In Figure 2, we present the H21 α spectrum integrated over the MonR2-IRS2 continuum source (Figure 1). Consistent with the H30 α and H26 α lines measured with the SMA (Jiménez-Serra et al. 2013), the H21 α transition shows two emission

⁵ The uncertainty in α considers the rms noise and systematic errors ($\leq 5\%$) in the SMA data. Note that the MonR2-IRS2 continuum flux in both SMA VEX and COM images differs by 2% (Table 2 in Jiménez-Serra et al. 2013).

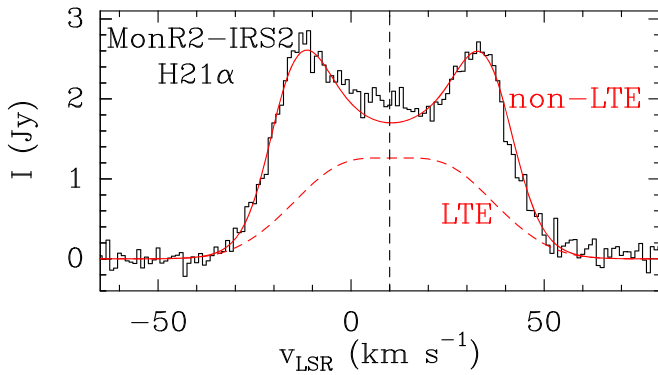


Figure 2. H21 α RRL profile (histogram) integrated over the MonR2-IRS2 source. The spectra modeled using the MORELI code for LTE (red dashed line) and non-LTE conditions (red solid line), are also shown (Section 4). The vertical dashed line indicates the systemic velocity at $v_{\text{LSR}} = 10 \text{ km s}^{-1}$.

peaks shifted by $\pm 22 \text{ km s}^{-1}$ with respect to MonR2-IRS2’s radial velocity at 10 km s^{-1} (Torrelles et al. 1983). The intensity of the two peaks is about the same ($\sim 2.8 \text{ Jy}$) and a factor of 10 higher than that of the H30 α RRL ($\sim 0.28 \text{ Jy beam}^{-1}$; Table 2 in Jiménez-Serra et al. 2013).⁶ This intensity increase is expected since the line-to-continuum flux ratio (LTCR)⁷ of RRLs under LTE conditions and optically thin emission is known to increase with frequency as $\nu^{1.1}$. The LTCR is predicted to be $\sim 206 \text{ km s}^{-1}$ for the H21 α line. However, the measured one is $\sim 1130 \text{ km s}^{-1}$, which clearly exceeds the LTCR predicted under LTE. This, together with our RRL radiative transfer calculations of Section 4, confirm that the RRLs at $\lambda \leq 0.85 \text{ mm}$ toward MonR2-IRS2 are masers.

Figure 1 reports the integrated intensity maps for the H21 α blueshifted and redshifted peaks from -20 to -5 km s^{-1} and from 25 to 40 km s^{-1} , respectively (middle panel), and for the high-velocity blue and red wings (from -35 to -29 km s^{-1} and from 48 to 50 km s^{-1} respectively; right panel). The H21 α maps of the emission peaks follow the morphology of the continuum (left panel), but their maxima are displaced by $\sim 0''.02$ ($\sim 18 \text{ au}$) from the continuum peak. While the redshifted emission peaks toward the northwest of MonR2-IRS2, the blueshifted part peaks toward the southeast. As shown in Section 4, this emission is well reproduced by a Keplerian ionized disk. For the high-velocity wings, the H21 α line follows a similar kinematic trend (redshifted gas in the northwest, blueshifted emission in the southeast), but its morphology appears slightly elongated in the direction perpendicular to the disk (see the dashed line in Figure 1, right panel), as if an ionized wind were launched from the disk (Sections 3.3 and 4).

3.3. H21 α Centroid Map

The bright emission of the H21 α masers allows us to investigate the kinematics and internal structure of MonR2-IRS2 with an exquisite accuracy. For this, we have constructed the centroid map of the H21 α emission in 5 km s^{-1} channels using 2D Gaussians (Figure 3, black crosses and filled circles).

⁶ Note that the SMA beams ranged between $0''.4$ and $2''.4$, therefore the SMA data include all emission from the MonR2-IRS2 source (size $\leq 60 \text{ mas}$; Section 3.1).

⁷ The LTCR is defined as $\frac{\Delta v T_L}{T_C}$, with Δv and T_L being, respectively, the line width and peak intensity of the RRL and T_C the free-free continuum flux.

The typical errors in the centroid positions (error bars in Figure 3) are $1\text{--}2 \text{ mas}$ ($0.9\text{--}1.8 \text{ au}$) for velocities between -20 and 40 km s^{-1} . Note that positional errors are also a function of the errors in the bandpass calibration (Zhang et al. 2017). However, the phase noise in the ALMA bandpass data was $\leq 1^\circ$, which implies a negligible effect in the positional errors of the H21 α centroids.

Figure 3 shows that for velocities between -8 and 32 km s^{-1} , the H21 α centroids are distributed along an almost perfect line in the northwest-southeast direction. The centroids, however, depart from this line at high velocities, especially for the blueshifted gas ($\leq -8 \text{ km s}^{-1}$), although some of the associated positional errors are large. This suggests the presence of a second kinematic component. As shown in Section 4, this configuration is consistent with the presence of an almost edge-on ionized disk, and a disk wind.

4. Modeling of the H21 α RRL

Similar configurations to the RRL centroid map obtained for MonR2-IRS2 have been observed for MWC349A (Martín-Pintado et al. 2011; Báez-Rubio et al. 2013; Zhang et al. 2017) and MWC922 (Sánchez Contreras et al. 2019). This configuration has been modeled assuming that the massive star is surrounded by a (partly) ionized Keplerian disk and an ionized wind. We have thus adopted a similar physical structure to model the H21 α centroid map derived for MonR2-IRS2. The set of input parameters that best fit our ALMA observations is described below (see also Table 1).

In our model, the ionized wind lies inside a double cone with a semi-opening angle of 57° (the neutral disk), while the ionized disk layer is contained within an opening angle of 6.5° on the surface of the double cone (Figure 4). The ionized wind expands radially at a constant velocity, v_0 , while the circumstellar disk rotates following a Keplerian law with the velocity rotation component being added to the expansion velocity of the wind (Martín-Pintado et al. 2011; Báez-Rubio et al. 2013). The inclination angle is measured from the direction perpendicular to the disk and is -25° .

We have used the non-LTE 3D radiative transfer code MORELI (MOdel for REcombination LInes; Báez-Rubio et al. 2013) and the departure coefficients of hydrogen, b_n and β_n , calculated by Walmsley (1990). The velocity separation between the H21 α emission peaks (blueshifted and redshifted; Figure 2) constrains the central mass of the MonR2-IRS2 source to $15 M_\odot$. This mass corresponds to a B0-type star on the zero-age main sequence, which is consistent with the luminosity of MonR2-IRS2 ($\sim 0.5\text{--}1 \times 10^4 L_\odot$; Howard et al. 1994).

The radial density distribution of electrons within the ionized double cone, N_e , follows a r^{-2} law with an inner radius of 13 au (Table 1). We choose a r^{-2} law because it fits nicely the 1.3, 0.85 and 0.4 mm free-free continuum fluxes of MonR2-IRS2, and it allows us to simultaneously model the disk and the expanding wind in a simple way. The predicted mass-loss rate for MonR2-IRS2 is $2.8 \times 10^{-7} M_\odot \text{ yr}^{-1}$, and the mass of the ionized disk is $2.4 \times 10^{-5} M_\odot$, a factor ≥ 10 lower than the neutral disk mass ($\sim 2\text{--}4 \times 10^{-4} M_\odot$; Section 3.1).

The electron temperature, T_e , that best fits our ALMA data is 5850 K . This value is lower than those typically measured in H II regions ($\sim 8000 \text{ K}$). However, note that T_e can only be constrained using RRL thermal emission. The expanding velocity of the ionized wind is 10 km s^{-1} , with a turbulent

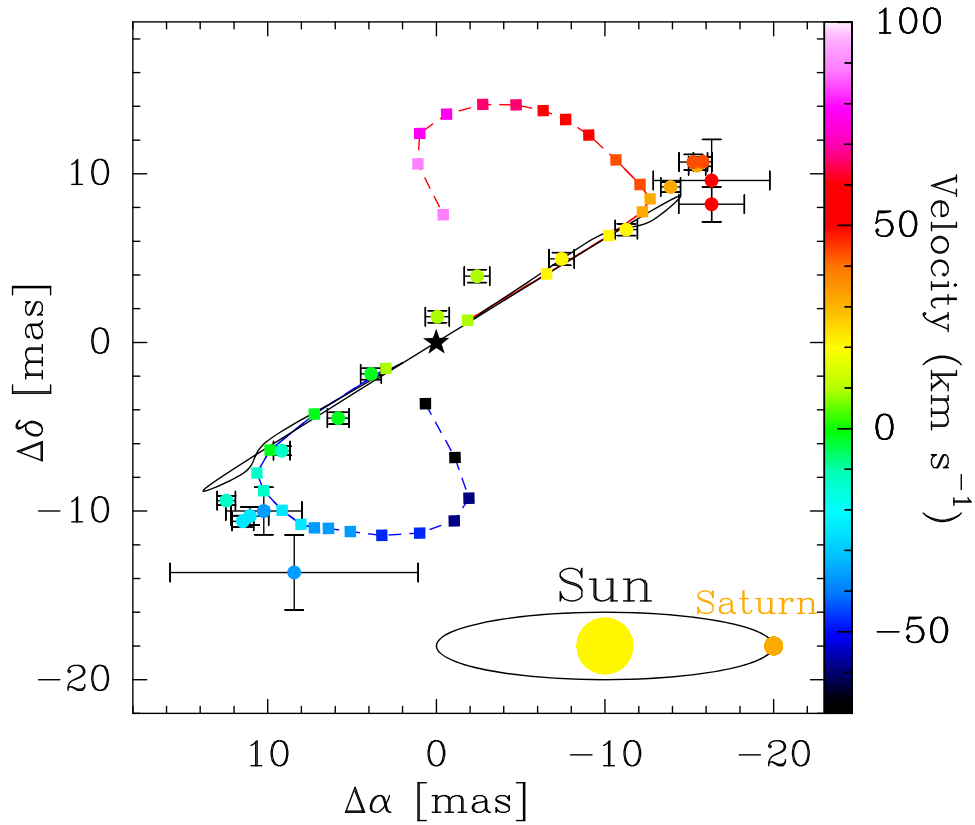


Figure 3. H21 α centroid map obtained toward MonR2-IRS2 after subtracting the central coordinates of the source. The crosses and filled circles represent the derived 2D Gaussian centroids, and the color scale shows the velocity associated with each centroid position. The error bars correspond to the $\pm 1\sigma$ positional error from the centroid fitting. The colored lines and squares report the H21 α centroid positions and velocities predicted by the MORELI code, assuming an ionized disk and disk wind for the physical structure of MonR2-IRS2. The dashed lines show the model predictions for the velocity ranges where the signal-to-noise ratio in the ALMA data is low. The black line reports the MORELI predictions for the same model but without a wind. 10 mas corresponds to 9 au, the Sun-Saturn distance.

Table 1

Input Parameters of the Best Fit of the MonR2-IRS2 H21 α Data

Parameter	Value
Central mass, M_*	$15 M_\odot$
Density distribution ^a , $N_c(r, \theta)$	$5.36 \times 10^7 r^{-2} \exp[(\theta - \theta_a)/20] \text{ cm}^{-3}$
Inner radius, r_{\min}	13 au
Double-cones semi-opening, θ_a	57°
Electron temperature, T_e	5850 K
Inclination angle, θ_i	-25°
Opening angle of the ionized disk, θ_d	6.5°
Outflow terminal velocity, v_0	10 km s^{-1}
Outflow turbulent velocity, v_{tu}	5 km s^{-1}
Mass-loss rate, \dot{M}	$2.8 \times 10^{-7} M_\odot \text{ yr}^{-1}$
Mass of the ionized disk, m_d	$2.4 \times 10^{-3} M_\odot$

Note.

^a r is in units of 15 au and angles are measured relative to the polar axis; θ and θ_a , are in degrees.

component of 5 km s^{-1} . Expansion velocities $\geq 20 \text{ km s}^{-1}$ are ruled out because the predicted H21 α line widths in the wings would be too large. As shown below, the absence of an expanding wind cannot explain the departure of the H21 α centroids from the disk plane observed at high velocities (especially blueshifted ones).

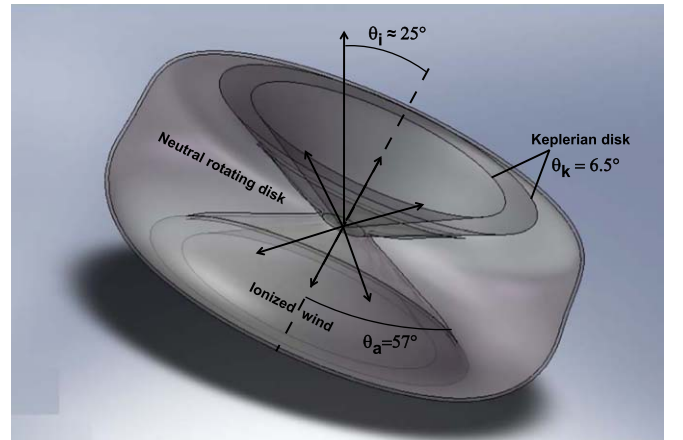


Figure 4. Sketch of the double-cone geometry used for the modeling of MonR2-IRS2 (see also Martín-Pintado et al. 2011; Báez-Rubio et al. 2013).

Our model fits very well the H21 α RRL profile measured toward MonR2-IRS2 (red line, Figure 2). A comparison between the LTE and non-LTE cases⁸ reveals that non-LTE effects need to be invoked to explain the H21 α double-peaked profile. For the H30 α and H26 α RRLs, the model predicts peak intensities a factor of ~ 2 higher than observed. However, we note that RRL masers are highly variable (Thum et al. 1992).

⁸ The LTE spectrum is obtained by fixing b_n and β_n to 1.

The H21 α centroid distribution predicted by our model also nicely matches that measured with ALMA (color lines and filled squares; Figure 3). The Keplerian component reproduces fairly well the kinematics of H21 α emission along the disk plane. The observations, however, reveal small deviations with respect to the model at velocities 2, 12, and 17 km s⁻¹ (such deviations are larger than the centroids positional errors), as if the disk were warped. Disk warping may appear in systems presenting a secondary object such as a stellar companion or a massive planet (Nealon et al. 2018; Kraus et al. 2020). This would be consistent with the fact that the modeled electron density distribution of MonR2-IRS2 requires an internal hole of radius 13 au. This was already noted by Jiménez-Serra et al. (2013) since, unlike MWC349A, the free-free continuum emission of MonR2-IRS2 at $\lambda \leq 1.3$ mm is optically thin. Alternatively, the warping of the disk could be produced by anisotropic accretion of gas (Sakai et al. 2019) or by a misalignment between the disk rotation axis and the magnetic field direction (Ciardi & Hennebelle 2010).

From Figure 3, we also find that the ionized gas at high velocities (mostly blueshifted) departs from the disk plane at distances ~ 12 mas from the disk center. This departure can only be explained by the presence of an ionized wind launching at radii ~ 11 au. Indeed, the same model but without a wind, does not reproduce such deviations (black line in Figure 3). As found toward other sources (MWC349A or MWC922; Martín-Pintado et al. 2011; Báez-Rubio et al. 2013; Zhang et al. 2017; Sánchez Contreras et al. 2019), launching radii of ~ 10 au are consistent with magnetically-regulated disk wind models (Blandford & Payne 1982) rather than with X-wind theory (Shu et al. 1994). Disk UV photoevaporation cannot be responsible either for the formation of the disk wind in MonR2-IRS2 because its gravitational radius, r_g (the distance at which photoevaporating disk winds are launched; Hollenbach et al. 1994), is ~ 100 au, i.e., 10 times larger than that observed in MonR2-IRS2.

Alternatively, the departure of the high-velocity centroid positions could be due to a second warp in the outer disk of MonR2-IRS2. However, as shown by Nealon et al. (2018), the disk twist produced by a companion such as a massive planet can go up to 60°. This value is smaller than the putative disk twist observed for MonR2-IRS2 ($>90^\circ$, Figure 3).

Finally, note that the model used here is different from the one proposed by Jiménez-Serra et al. (2013). The previous model was motivated by the asymmetry of the H26 α RRL detected toward MonR2-IRS2 with the SMA. Such an asymmetry is not observed in the H21 α line (Section 3.2), which suggests that the H26 α maser may be variable. Variability is common in RRL masers since their line profiles can change on timescales as short as 30 days (see MWC349A; Martín-Pintado et al. 1989b; Thum et al. 1992). Future ALMA observations will reveal whether or not the H26 α line asymmetry detected with the SMA was transitory.

5. Conclusions

Sections 3 and 4 show that RRL masers are powerful tools to unveil the kinematics and physical structure of the innermost regions around massive stars. Indeed, RRL masers are very sensitive to the electron density distribution, geometry, electron temperature, and kinematics of the ionized gas (Strelitski et al. 1996; Báez-Rubio et al. 2013, 2014). Regardless of their evolutionary stage, all RRL maser objects firmly detected to

date (MWC349A, MWC922 and MonR2-IRS2; Martín-Pintado et al. 2011; Báez-Rubio et al. 2013; Sánchez Contreras et al. 2019, and this work) present the same physical structure for the ionized gas: a circumstellar disk rotating in a Keplerian fashion, and an expanding ionized wind launched at distances of tens of astronomical units that follows the same Keplerian rotation. This disk+wind geometry may thus be the optimized configuration for RRL masers to form.

We thank the anonymous referee for the constructive comments. This Letter makes use of the ALMA data ADS/JAO.ALMA 2012.1.00522.S. ALMA is a partnership of ESO (representing its member states), NSF (USA) and NINS (Japan), together with NRC (Canada), NSC and ASIAA (Taiwan), and KASI (Republic of Korea), in cooperation with the Republic of Chile. The Joint ALMA Observatory is operated by ESO, AUI/NRAO, and NAOJ. I.J.-S., A.B.-R., and J.M.-P. acknowledge support from the Spanish FEDER (project number ESP2017-86582-C4-1-R) and the State Research Agency (AEI; project number PID2019-105552RB-C41). V.M.R. has received funding from the EU Horizon 2020 program under the Marie Skłodowska-Curie grant agreement No. 664931. We thank A. Richards for the help provided during the calibration/imaging of the data.

ORCID iDs

Izaskun Jiménez-Serra  <https://orcid.org/0000-0003-4493-8714>

Qizhou Zhang  <https://orcid.org/0000-0003-2384-6589>

Víctor M. Rivilla  <https://orcid.org/0000-0002-2887-5859>

References

- Álvarez, C., Hoare, M., Glindemann, A., & Richichi, A. 2004, *A&A*, 427, 505
 Añez-López, N., Osorio, M., Busquet, G., et al. 2020, *ApJ*, 888, 41
 Báez-Rubio, A., Martín-Pintado, J., Thum, C., & Planesas, P. 2013, *A&A*, 553, A45
 Báez-Rubio, A., Martín-Pintado, J., Thum, C., Planesas, P., & Torres-Redondo, J. 2014, *A&A*, 571, L4
 Blandford, R. D., & Payne, D. G. 1982, *MNRAS*, 199, 883
 Bonnell, I., & Bate, M. 2006, *MNRAS*, 370, 488
 Carpenter, J. M., Meyer, M. R., Dougados, C., Strom, S. E., & Hillenbrand, L. A. 1997, *AJ*, 114, 198
 Cesaroni, R., Galli, D., Neri, R., & Walmsley, C. 2014, *A&A*, 566, A73
 Chen, H.-R. V., Keto, E., Zhang, Q., et al. 2016, *ApJ*, 823, 125
 Churchwell, E. 2002, *ARA&A*, 40, 27
 Ciardi, A., & Hennebelle, P. 2010, *MNRAS*, 409, L39
 Cox, P., Martín-Pintado, J., Bachiller, R., et al. 1995, *A&A*, 295, L39
 Dzib, S. A., Ortiz-León, G. N., Loinard, L., et al. 2016, *ApJ*, 826, 201
 Gvaramadze, V. V., & Menten, K. M. 2012, *A&A*, 541, A7
 Hartmann, L., Jaffe, D., & Huchra, J. P. 1980, *ApJ*, 239, 905
 Hollenbach, D., Johnstone, D., Lizano, S., & Shu, F. 1994, *ApJ*, 428, 654
 Howard, E. M., Pipher, J. L., & Forrest, W. J. 1994, *ApJ*, 425, 707
 Jaffe, D. T., & Martín-Pintado, J. 1999, *ApJ*, 520, 162
 Jiménez-Serra, I., Báez-Rubio, A., Rivilla, V. M., et al. 2013, *ApJL*, 764, L4
 Jiménez-Serra, I., Martín-Pintado, J., Caselli, P., et al. 2009, *ApJ*, 703, L157
 Jiménez-Serra, I., Martín-Pintado, J., Rodríguez-Franco, A., et al. 2007, *ApJ*, 661, L187
 Keto, E. 2007, *ApJ*, 666, 976
 Kraus, M., Arias, M. L., Cidale, L. S., & Torres, A. F. 2020, *MNRAS*, 493, 4308
 Kraus, S., Kreplin, A., Young, A. K., et al. 2020, *Sci*, submitted (arXiv:2004.01204)
 Martín-Pintado, J., Bachiller, R., Thum, C., & Walmsley, M. 1989a, *A&A*, 215, L13
 Martín-Pintado, J., Thum, C., & Bachiller, R. 1989b, *A&A*, 222, L9
 Martín-Pintado, J., Thum, C., Planesas, P., et al. 2011, *A&A*, 530, L15
 Massi, M., Felli, M., & Simon, M. 1985, *A&A*, 152, 387
 Maud, L. T., Cesaroni, R., Kumar, M. S. N., et al. 2019, *A&A*, 627, L6

- McKee, C., & Tan, J. 2002, *Natur*, 416, 59
- Nealon, R., Dipierro, G., Alexander, R., Martin, R. G., & Nixon, C. 2018, *MNRAS*, 481, 20
- Ossenkopf, V., & Henning, T. 1994, *A&A*, 291, 943
- Patel, N. A., Curiel, S., Sridharan, T. K., et al. 2005, *Natur*, 437, 109
- Sai, J., Ohashi, N., Saigo, K., et al. 2020, *ApJ*, 893, 51
- Sakai, N., Hanawa, T., Zhang, Y., et al. 2019, *Natur*, 565, 206
- Sánchez Contreras, C., Báez-Rubio, A., Alcolea, J., et al. 2019, *A&A*, 629, A136
- Shu, F., Najita, J., Ostriker, E., et al. 1994, *ApJ*, 429, 781
- Strelitski, V., Bieging, J. H., Hora, J., et al. 2013, *ApJ*, 777, 89
- Strelitski, V. S., Ponomarev, V. O., & Smith, H. A. 1996, *ApJ*, 470, 1118
- Thum, C., Martín-Pintado, J., & Bachiller, R. 1992, *A&A*, 256, 507
- Torrelles, J. M., Rodríguez, L. F., Cantó, J., et al. 1983, *ApJ*, 274, 214
- Treviño-Morales, S. P., Fuente, A., Sánchez-Monge, Á., et al. 2019, *A&A*, 629, A81
- Walmsley, C. M. 1990, *A&AS*, 82, 201
- Weintraub, J., Moran, J. M., Wilner, D. J., et al. 2008, *ApJ*, 677, 1140
- Wood, D. O. S., & Churchwell, E. 1989, *ApJS*, 69, 831
- Zhang, Q., Claus, B., Watson, L., & Moran, J. 2017, *ApJ*, 837, 53